

Coverage Axis++: Efficient Inner Point Selection for 3D Shape Skeletonization

ZIMENG WANG*, The University of Hong Kong, China

ZHIYANG DOU*, The University of Hong Kong, China; University of Pennsylvania, USA

RUI XU, Shandong University, China

CHENG LIN, The University of Hong Kong, China

YUAN LIU, The University of Hong Kong, China

XIAOXIAO LONG, The University of Hong Kong, China

SHIQING XIN, Shandong University, China

LINGJIE LIU, University of Pennsylvania, USA

TAKU KOMURA, The University of Hong Kong, China

XIAOMING YUAN†, The University of Hong Kong, China

WENPING WANG†, Texas A&M University, USA

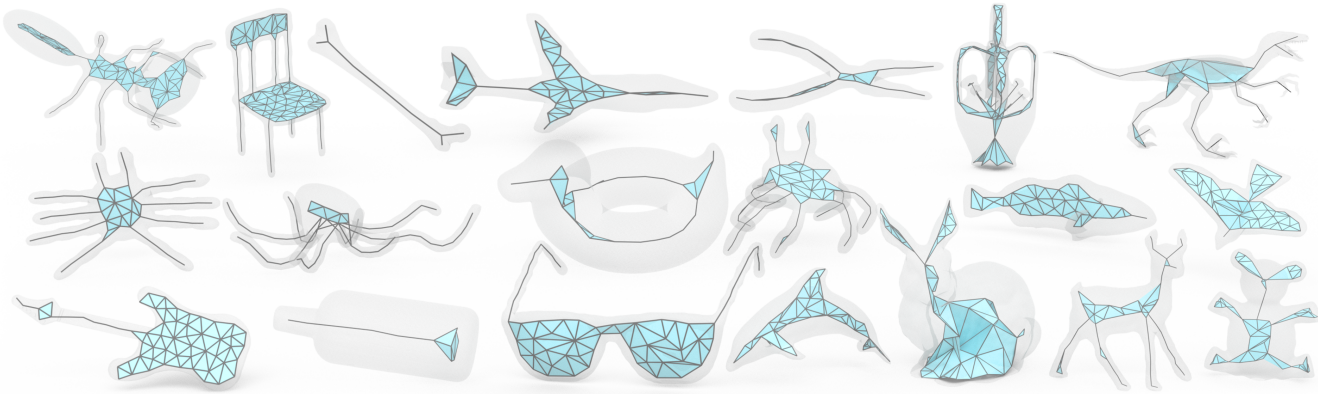


Fig. 1. Coverage Axis++ enables highly efficient skeletonization of the given shapes represented by water-tight meshes, triangle soups or point clouds. Compared with the SOTA method [Dou et al. 2020; Li et al. 2015; Lin et al. 2021], Coverage Axis++ allows for fast medial axis approximation with low reconstruction error, i.e., Coverage Axis++: 5.362% reconstruction error in 2.9s v.s. Coverage Axis: 6.574% reconstruction error in 236.1s on average; See Tab. 1.

We introduce Coverage Axis++, a novel and efficient approach to 3D shape skeletonization. The current state-of-the-art approaches for this task often

*Equal Contribution.

†Equal Advising.

Authors' addresses: Zimeng Wang, wzm2000@connect.hku.hk, The University of Hong Kong, China; Zhiyang Dou, zhiyang0@connect.hku.hk, The University of Hong Kong, China; and University of Pennsylvania, USA; Rui Xu, xrvtid@163.com, Shandong University, China; Cheng Lin, chlin@connect.hku.hk, The University of Hong Kong, China; Yuan Liu, yuanly@connect.hku.hk, The University of Hong Kong, China; Xiaoxiao Long, xxlong@connect.hku.hk, The University of Hong Kong, China; Shiqing Xin, xinshiqing@sdu.edu.cn, Shandong University, China; Lingjie Liu, lingjie.liu@seas.upenn.edu, University of Pennsylvania, USA; Taku Komura, taku@cs.hku.hk, The University of Hong Kong, China; Xiaoming Yuan, xmyuan@hku.hk, The University of Hong Kong, China; Wenping Wang, wenping@tamu.edu, Texas A&M University, USA.

Permission to make digital or hard copies of all or part of this work for personal or classroom use is granted without fee provided that copies are not made or distributed for profit or commercial advantage and that copies bear this notice and the full citation on the first page. Copyrights for components of this work owned by others than ACM must be honored. Abstracting with credit is permitted. To copy otherwise, or republish, to post on servers or to redistribute to lists, requires prior specific permission and/or a fee. Request permissions from permissions@acm.org.

© 2024 Association for Computing Machinery.

XXXX-XXXX/2024/2-ART \$15.00

<https://doi.org/10.1145/nnnnnnn.nnnnnnn>

rely on the watertightness of the input [Li et al. 2015] or suffer from substantial computational costs [Dou et al. 2022], thereby limiting their practicality. To address this challenge, Coverage Axis++ proposes a heuristic algorithm to select skeletal points, offering a high-accuracy approximation of the Medial Axis Transform (MAT) while significantly mitigating computational intensity for various shape representations. We introduce a simple yet effective strategy that considers both shape coverage and uniformity to derive skeletal points. The selection procedure enforces consistency with the shape structure while favoring the dominant medial balls, which thus introduces a compact underlying shape representation in terms of MAT. As a result, Coverage Axis++ allows for skeletonization for various shape representations (e.g., water-tight meshes, triangle soups, point clouds), specification of the number of skeletal points, few hyperparameters, and highly efficient computation with improved reconstruction accuracy. Extensive experiments across a wide range of 3D shapes validate the efficiency and effectiveness of Coverage Axis++. The code will be publicly available once the paper is published.

CCS Concepts: • **Computing methodologies** → **Shape analysis; Point-based models; Mesh geometry models.**

Additional Key Words and Phrases: medial axis transform, medial surface, skeletonization, shape analysis

ACM Reference Format:

Zimeng Wang, Zhiyang Dou, Rui Xu, Cheng Lin, Yuan Liu, Xiaoxiao Long, Shiqing Xin, Lingjie Liu, Taku Komura, Xiaoming Yuan, and Wenping Wang. 2024. Coverage Axis++: Efficient Inner Point Selection for 3D Shape Skeletonization. 1, 1 (February 2024), 13 pages. <https://doi.org/10.1145/nmnnmnnm.nmnnmnnm>

1 INTRODUCTION

Skeletal representations have become a popular tool in various applications of shape analysis and geometric processing, as they efficiently capture the underlying structures of 3D shapes. Skeletal representations have been widely adopted for various downstream tasks including 3D reconstruction [Amenta et al. 2001; Tang et al. 2019; Wu et al. 2015], volume approximation [Stolpner et al. 2011; Sun et al. 2013], shape segmentation [Lin et al. 2020], shape abstraction [Dou et al. 2020], pose estimation [Shotton et al. 2011; Yang et al. 2021], and animation [Baran and Popović 2007; Yang et al. 2018], among others.

Previous efforts have been made for the computation of curve skeleton [Au et al. 2008; Ma et al. 2003; Tagliasacchi et al. 2012; Xu et al. 2019], which consists of only 1D curves. While Dey and Sun [Dey and Sun 2006] provide a mathematical definition based on the Medial Geodesic Function, curve skeletons are generally empirically understood. Moreover, the curve representation is typically limited to tubular components and cannot be considered a generalized tool for shape analysis.

Another popular skeletal representation is the Medial Axis Transform (MAT) [Blum et al. 1967]. The MAT is defined by a union of maximally inscribed balls within the shape, along with their associated radius functions. A formal definition of MAT is given in Sec. 3.1. Different from the curve skeleton, the MAT has a consistent definition for arbitrary shapes. It comprises both curve-like and surface-like structures, leading to a significantly better representational ability.

As of yet, the MAT computation poses challenges due to sensitivity to boundary noise and strict input geometry requirements, e.g., watertightness and manifoldness of the surface [Li et al. 2015]. To tackle the problem, an effective method named Coverage Axis [Dou et al. 2022] is introduced to model skeletal point selection as a Set Cover Problem. It aims to identify the smallest sub-collection covering the entire shape. This method minimizes dilated inner balls to approximate the shape, establishing a correspondence between the skeleton and the shape, leading to a compact representation of the original shape. However, solving the Coverage Axis is time-consuming since it is in an SCP format, which is a well-known NP-hard problem. For instance, the average running time of the Coverage Axis can be 236.1s with the standard deviation being 408.4s; See Tab. 1.

In this paper, we develop a simple yet more efficient method for shape skeletonization. We take centrality and uniformity into consideration and sidestep the expensive coverage constraint by developing a heuristic algorithm to achieve representative skeletal point selection with high efficiency. Specifically, we present a scoring scheme that assigns a score to each inner point as a quantification of its skeletal representation ability. The scoring consists of the *coverage score* and the *uniformity score*. The coverage score is

determined by evaluating the number of surface samples that can be covered within the dilated ball associated with the candidate to ensure coverage. The coverage score enforces consistency with the shape structure while favoring the interior points that dominate a larger area, which corresponds to the definition of MAT, i.e., maximally inscribed spheres. The centrality of the skeleton is achieved by the coverage condition. On the other hand, uniformity is one of the key desired features of compact skeletonization without redundant structures, for which we introduce the uniformity score. The score is calculated by measuring the distance between the candidate and the nearest point in the set of selected inner points. This achieves a uniformly distributed skeletonization result by preventing the selected points from clustering together. The skeletal points are derived by running a priority queue defined by these two scores. This simple yet effective point selection manner produces a better abstraction of the overall shape as well as a shape-aware point distribution and sidesteps solving an optimization problem with high computation complexity. Notably, although the priority queue works in a greedy manner, Coverage Axis++ achieves global consistency between the skeleton and the original shape and allows for specifying different numbers of target skeletal points; See Sec. 6.1.

Compared with the existing methods [Amenta et al. 2001; Dey and Zhao 2002; Dou et al. 2022; Foskey et al. 2003; Giesen et al. 2009; Li et al. 2015; Miklos et al. 2010; Sud et al. 2007], this simple yet effective strategy allows for 1) skeletonization for various shape representations including water-tight meshes, triangle soups and point clouds; 2) specifying the number of skeletal points, which is a desirable feature for learning-based methods as a fixed number of points are typically required; 3) highly efficient computation while achieving better or more competitive reconstruction accuracy; 4) few hyperparameters; 5) randomly generated candidates inside the volume as it selects the most expressive ones from overfilled inner point candidates.

We conduct extensive experiments to demonstrate the effectiveness and robustness of our method on a variety of 3D shapes. The comprehensive evaluation reveals that our method effectively captures the underlying MATs with lower reconstruction errors while achieving much higher computation efficiency.

2 RELATED WORK

Efficient shape representation is essential for various geometric modeling and analysis tasks [Amenta et al. 2001; Dou et al. 2020; Fu et al. 2022; Lin et al. 2020, 2023; Liu et al. 2023b,a; Marschner et al. 2023; Sellán et al. 2021, 2020; Wen et al. 2023; Xin et al. 2016; Xu et al. 2023, 2022; Yang et al. 2023; Yariv et al. 2023; Yu et al. 2023; Zhang et al. 2023]. Skeletonization, as a popular choice in this regard, has been extensively studied in recent decades. We refer readers to [Tagliasacchi et al. 2016] for a detailed survey covering various forms of skeletons.

Curve Skeletonization. Many efforts have been made to curve skeletonization. Traditional approaches typically rely on hand-crafted rules to leverage geometric information to compute curved skeletons [Attali and Montanvert 1996; Au et al. 2008; Bærentzen and Rotenberg 2021; Cheng et al. 2020; Ma et al. 2003; Natali et al. 2011; Sharf et al. 2007; Tagliasacchi et al. 2012; Xu et al. 2019]. Ma et

al.[Ma et al. 2003] employ radial basis functions (RBFs) for extracting the skeleton. Sharf et al. [Sharf et al. 2007] utilize a deformable model evolution that captures the volumetric shape of the object, subsequently generating an approximation for the curve skeleton. Au et al.[Au et al. 2008] compute the skeleton through mesh extraction. Tagliasacchi et al. [Tagliasacchi et al. 2012] formulate the skeletonization problem using mean curvature flow (MCF) and incorporate external energy terms to generate the curve skeleton.

Livesu et al.[Livesu et al. 2012] use the visual hull for 3D shape curve skeleton reconstruction. Mean Curvature Skeleton[Tagliasacchi et al. 2012] employs mean curvature flow to collapse the input mesh, generating a meso-skeleton with surface-like and curve-like structures. Cheng et al. [Cheng et al. 2020] propose skeletonization using the dual of shape segmentation. Learning-based methods, as proposed in [Xu et al. 2019], aim to predict curve skeletons. However, these skeletons face challenges in accurately representing arbitrary shapes, particularly those with flat components.

Medial Axis Transform. The Medial Axis Transform (MAT), as a more general skeletal representation, encodes shapes with curve-like and mesh-like structures by representing them through maximal balls with varying radii. It can be viewed as a discrete Minkowski sum, providing a concise mathematical description of the shape.

Efforts in MAT computation have been extensive [Amenta et al. 2001; Dey and Zhao 2002; Dou et al. 2022; Foskey et al. 2003; Ge et al. 2023; Hu et al. 2022, 2023; Rebain et al. 2021; Sud et al. 2007; Wang et al. 2022a]. Angle-based filtering methods [Amenta et al. 2001; Dey and Zhao 2002; Foskey et al. 2003; Sud et al. 2007] simplify based on the angle formed by a point of MA and its two closest boundary points, preserving local features but compromising original topology. λ -medial axis methods [Chaussard et al. 2011; Chazal and Lieutier 2005] use cumradius of closest points as a pruning criterion but struggle with feature preservation at different scales [Attali et al. 2009]. Scale Axis Transform [Miklos et al. 2010] excels in spike pruning but is limited by high computational cost and topology disruption. Progressive medial axis [Faraj et al. 2013] proposes to perform successive edge collapse based on sphere absorption to preserve the topology as well as improve time efficiency. Besides, many strategies have been proposed for MAT simplification including Delta Medial Axis (DMA)[Marie et al. 2016], Bending Potential Ratio pruning[Shen et al. 2011], Erosion Thickness measure [Yan et al. 2016], and voxelization-based λ -pruning[Yan et al. 2018]. Sun et al.[Sun et al. 2013] propose to control the approximation error through Hausdorff distance. Li et al. [Li et al. 2015] propose Q-MAT for highly accurate shape approximation, utilizing a quadratic error metric [Garland and Heckbert 1997] during simplification. However, Q-MAT is limited to 2-manifold surfaces. Besides, Q-MAT is sensitive to the quality of MAT initialization. Recently, Wang et al. [Wang et al. 2022a] compute MAT with well-preserved geometric features via the Restricted power diagram.

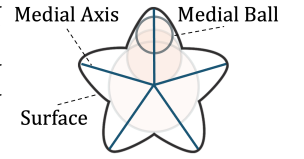
Point Cloud Skeletonization. Point cloud skeletonization has gained attention due to the widespread availability of point cloud data [Andrea Tagliasacchi 2009; Cao et al. 2010; Huang et al. 2013; Livesu et al. 2012; Rebain et al. 2019; Wu et al. 2015; Yang et al. 2020]. The L1-medial skeleton [Huang et al. 2013] contracts point clouds using locally optimal projections [Lipman et al. 2007]. LSMAT[Rebain

et al. 2019] approximates the MAT based on the Signed Distance Function from a densely sampled oriented point set. Wu et al.[Wu et al. 2015] link surface points to the inner point on the meso-skeleton[Tagliasacchi et al. 2012], but their unstructured point representation lacks topological constraints, leading to high reconstruction errors. With the rise of deep learning, learning-based skeletonization methods for point clouds have emerged [Ge et al. 2023; Lin et al. 2021; Yang et al. 2020]. Point2Skeleton [Lin et al. 2021] learns skeletal representations from generalized point clouds. However, learning-based methods may lack accuracy in computing geometric features and face challenges in generalization due to dependency on training data as we will demonstrate.

3 PRELIMINARIES

3.1 Medial Surface

For a closed, oriented, and bounded two-manifold surface \mathcal{S} in \mathbb{R}^3 , the *medial axis* is defined as the locus of the centers of *maximally inscribed spheres* (medial balls) that are tangent to \mathcal{S} at two or more points. Denoted by a pair $(\mathcal{M}, \mathcal{R})$, where \mathcal{M} is the medial axis of \mathcal{S} and \mathcal{R} is its radius function, the combination forms the *medial axis transform* (MAT).



3.2 Voronoi Diagram & Power Diagram

Voronoi Diagram (VD) is a partition of the domain $\Omega \subset \mathbb{R}^d$ into regions, close to a set of points called generators $\{x_i \in \Omega\}_{i=1}^n$. Each region, also called cell, is defined as

$$\Omega_i^{\text{vor}} : \{x \in \Omega \mid \|x - x_i\| \leq \|x - x_j\|, j \neq i\}.$$

A well-known MAT initialization technique is to use the VD inside a shape generated by surface samples [Amenta et al. 2001; Dou et al. 2022; Li et al. 2015].

In Power Diagram (PD) [Aurenhammer 1987], each generator x_i is equipped with a weight w_i to control its influence. By defining the power distance $d^{\text{pow}}(x, x_i)$ between x and the weighted generator x_i to be $\|x - x_i\|^2 - w_i$, the cell associated with x_i is defined by

$$\Omega_i^{\text{pow}} : \{x \in \Omega \mid d^{\text{pow}}(x, x_i) \leq d^{\text{pow}}(x, x_j), j \neq i\}.$$

A generator with a larger weight is more dominant, and when weights are equal, the PD is reduced to a VD.

3.3 Coverage Axis

Coverage Axis [Dou et al. 2022] is an effective method for shape skeletonization of both meshes and point clouds, where the skeletal point selection problem is modeled as a set cover problem (SCP). Given candidate skeletal points $P = \{p_i\}$, the goal is to find the minimum number of dilated balls that cover all the sampled points $S = \{s_j\}$ on the surface. A coverage matrix $D \in \{0, 1\}^{m \times n}$ is used, where m and n are total numbers of sampled surface points and candidate skeletal points, respectively. Each entry $d_{ji} \in \{0, 1\}$ of D indicates if the surface point s_j is covered by the dilated ball (p_i, r'_i) :

$$d_{ji} = \begin{cases} 1, & \text{if } \|p_i - s_j\|_2 \leq r'_i, j = 1, \dots, m, i = 1, \dots, n \\ 0, & \text{if } \|p_i - s_j\|_2 > r'_i, j = 1, \dots, m, i = 1, \dots, n. \end{cases} \quad (1)$$

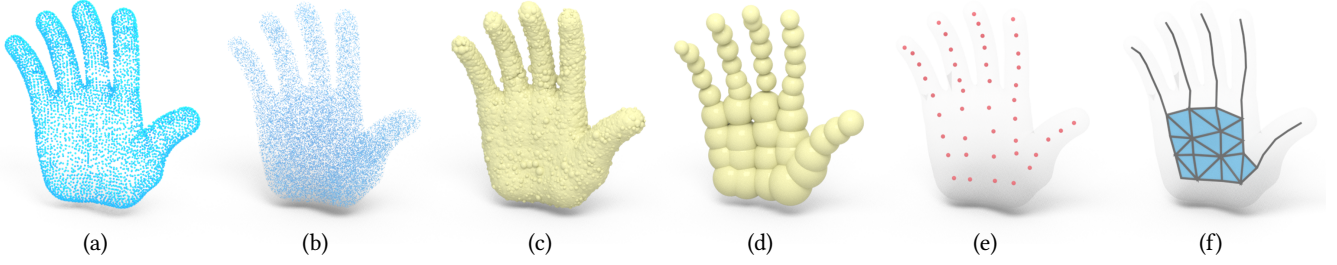


Fig. 2. The pipeline of Coverage Axis++. (a) Input point cloud. (b) Inner point candidates. (c) Candidate inner balls with original radius. (d) Selected inner balls with original radius. (e) Selected inner points. (f) Skeletonization Result.

Let $\mathbf{v} \in \{0, 1\}^{n \times 1}$ be a decision vector, where the i -th element $v_i \in \{0, 1\}$ indicates if the candidate skeletal point p_i is selected. Coverage Axis selects points by solving the following constrained 0-1 integer programming problem:

$$\begin{aligned} & \min \|\mathbf{v}\|_2 \\ & s.t. \quad \mathbf{D}\mathbf{v} \geq \mathbf{1}, \end{aligned} \quad (2)$$

where $\mathbf{1}$ is the vector of all ones and \geq is applied element-wise. The neat formulation achieves high-level abstraction and robustness to noise. However, SCP is a well-known NP-Hard problem [Hartmanis 1982] and its running time complexity is $O(|P|^2 2^{|S|})$ where $|P|$ and $|S|$ are the number of candidate inner points and surface points, respectively. As a result, the Coverage Axis suffers from a high computational cost; Refer to Tab. 1 and Appendix. A.3.

4 METHOD

In this section, we present our algorithm for the selection of skeletal points, which involves a set of candidate points denoted as $P = \{p_i\}$, and a group of sampled points represented as $S = \{s_j\}$ on the surface. Each point is defined by its 3D Cartesian coordinates in \mathbb{R}^3 . In this paper, all inner point candidates are randomly generated inside the volume; See an example in Fig. 2 (b). The following steps outline our algorithm for skeletal point selection.

4.1 Preprocessing

Following [Dou et al. 2022], the first step is to compute the radii $R = \{r_i\}$ for the candidate points, where r_i is defined as the closest distance of p_i to the sampled surface set S , i.e.,

$$r_i := \text{dist}(p_i, S) = \min_{s_j \in S} \|p_i - s_j\|. \quad (3)$$

The set R together with the center points P define the candidate balls. We slightly dilate all the balls by a small factor to their radii, by *offset* or *scale*, namely,

$$r'_i = r_i + \delta_r \quad \text{or} \quad r'_i = r_i(1 + \delta_r), \quad (4)$$

leading to a set of dilated balls $B = \{B_i\}$, where B_i is the ball centered at p_i with radius r'_i . According to Eq. 1, we compute the coverage matrix $\mathbf{D} = (d_{ji}) \in \mathbb{R}^{m \times n}$, where $d_{ji} \in \{0, 1\}$ takes the value 1 if the surface point s_j is covered by the dilated ball B_i and 0 otherwise.

4.2 Coverage Score

To achieve compact skeletonization, we aim to select representative skeletal points that capture the key features of the given 3D object.

If the dilated ball B_i of a candidate point p_i can cover lots of surface samples from the surface point set S , p_i should be regarded as representative. This idea matches the one used in [Dou et al. 2022] in the sense that if the minimum number of skeletal points is selected by solving SCP, then the dilated ball of each selected point should cover lots of surface samples.

During the implementation of our algorithm, we denote by P^+ the set of selected skeletal points and P^- the set of unselected ones, such that $P = P^+ \cup P^-$ always holds. We also record the uncovered sampled surface points as S' , which consists of those uncovered surface samples, i.e.,

$$S' := \{s_j \in S \mid s_j \notin B_i, \forall p_i \in P^+\}. \quad (5)$$

Then, we assign a *coverage score* to each $p_i \in P^-$, which is determined by the number of samples in S' that B_i covers. With the help of the coverage matrix \mathbf{D} in an *offset* manner of Eq. 4, we formally define the coverage score of $p_i \in P^-$ as follows

$$\text{Cove}_i := \sum_{j: s_j \in S'} d_{ji}. \quad (6)$$

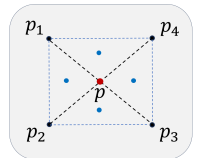
The introduced coverage score promotes a high coverage rate (See Appendix. A.2) of the overall shape to effectively enforce consistency with the given shape structure while favoring the interior points that dominate a larger area, leading to a compact representation of the input shape in the sense of MAT.

4.3 Uniformity Score

The coverage score intrinsically relates the skeletal points with the model surface, we also need another metric to guarantee the uniformity among the selected skeletal points. In other words, the selected points themselves should be relatively uniformly distributed in the space instead of forming groups. For this purpose, we introduce the *uniformity score* which aims at punishing those candidate points close to the set of currently selected points P^+ . Specifically, for each $p_i \in P^-$, its uniformity score is defined as

$$\text{Unif}_i := \text{dist}(p_i, P^+) = \min_{p_{i'} \in P^+} \|p_i - p_{i'}\|. \quad (7)$$

To illustrate the mechanics of the uniformity score defined above, consider skeletal point selection for a simple planar shape, where the p_1, p_2, p_3, p_4 are selected points within a rectangular shape. If not considering the effect of the coverage score, then according to Eq. 7, the next skeletal point p (highlighted in red) should be the intersection point of the line segments connecting p_1 and p_3 , as



well as p_2 and p_4 , ensuring that $\min_{i \in \{1,2,3,4\}} \|p - p_i\|$ is the largest within the rectangle, leading to the highest possible uniformity score for the selected point. Following this pattern, the subsequent four selected points (highlighted in blue) should be placed at the centroids of their respective triangles, resulting in a relatively uniform distribution of the selected skeletal points.

4.4 Final Score

We assign a final score to each candidate in $p_i \in P^-$ by combining its coverage score and uniformity score. We denote the two score vectors as $\mathbf{Cove} = (Cove_i)$ and $\mathbf{Unif} = (Unif_i)$, respectively. Since these two scores have different scales (one is in quantity units, and the other is in length units), we apply standardization to them. Specifically, for each $p_i \in P^-$, we perform the following transformation to $Cove_i$ and $Unif_i$

$$\begin{aligned} Cove_i &\leftarrow \frac{Cove_i - \text{mean}(\mathbf{Cove})}{\text{std}(\mathbf{Cove})} \\ Unif_i &\leftarrow \frac{Unif_i - \text{mean}(\mathbf{Unif})}{\text{std}(\mathbf{Unif})}, \end{aligned} \quad (8)$$

where $\text{mean}(\cdot)$ and $\text{std}(\cdot)$ represent the sample mean and sample standard deviation respectively. Then we add $Unif_i$ scaled by a weight parameter ω to $Cove_i$ to derive the final score for p_i , i.e.,

$$Score_i := Cove_i + \omega \cdot Unif_i. \quad (9)$$

After computing $Score_i$ for all $p_i \in P^-$, we select the candidate that achieves the highest score. An overview of the heuristic algorithm is summarized in Algorithm 1.

Algorithm 1: Coverage Axis++ for inner point selection

Input: sampled surface points S , candidate skeletal points P , dilation factor δ_r , weight parameter ω , target number of selected points $|V|$.

Result: the set of selected skeletal points P^+

Compute matrix \mathbf{D} based on Eq. 1, Initialize $S' = S$, $P^+ = \emptyset$, $P^- = P$ and $k = 1$;

while $S' \neq \emptyset$ and $k \leq |V|$ **do**

for $p_i \in P^-$ **do**

 Compute $Cove_i$ according to Eq. 6;

 Compute $Unif_i$ according to Eq. 7;

end

 Compute the mean and standard deviation for the two vectors $\mathbf{Cove} = (Cove_i)$ and $\mathbf{Unif} = (Unif_i)$;

for $p_i \in P^-$ **do**

 Standardize $Cove_i$ and $Unif_i$ according to Eq. 8;

 Compute $Score_i$ according to Eq. 9;

end

 Select $p_{i_k} \leftarrow \arg \min_{p_i \in P^-} \{Score_i\}$;

 Update $P^+ \leftarrow P^+ \cup \{p_{i_k}\}$, $P^- \leftarrow P^- \setminus \{p_{i_k}\}$;

 Update S' according to Eq. 5;

 Set $k \leftarrow k + 1$;

end

4.5 Connectivity of Skeletal Points

After selecting the skeletal points, we establish connections among them to produce the skeletonization result.

Mesh Input. Following [Amenta et al. 2001; Dou et al. 2022; Wang et al. 2022b], we initialize the candidate based on Voronoi diagram \mathbf{VD} . After selecting the skeletal points, we can obtain selected points embedded in the Voronoi diagram by nearest projection. We simplify \mathbf{VD} using the edge collapse strategy of Q-MAT [Li et al. 2015] following [Dou et al. 2022]. The simplification result \mathbf{VD}' serves as the final MAT of the given mesh input. Note topology preservation [Dey et al. 1998] and mesh inversion avoidance algorithm [Garland and Heckbert 1997] are applied during the edge collapse.

Point Cloud Input. As it is hard to preserve the topology during connection establishment for point clouds, we compute an approximation of the MAT connection following [Amenta et al. 2001]. We compute the Power diagram \mathbf{PD} on the set of $\{B'(p_i, r'_i), p_i \in P^+\} \cup \{B(s_j, \delta_r), s_j \in S\}$ where P^+ and S are sets of selected points and surface points, respectively. Then, the connectivity among skeletal points is obtained by extracting edges among the selected inner points on the dual of \mathbf{PD} , regular triangulation \mathbf{RT} (in other words, weighted alpha complexes). Note that r' can be adjusted accordingly during the computation of \mathbf{RT} to achieve flexible control over the connection [Amenta et al. 2001; Dou et al. 2022]. An overview of our pipeline is shown in Fig. 2.

4.6 Discussion

Complexity. Algorithm 1 has a polynomial complexity. Specifically, computing $Cove_i$ and $Unif_i$ costs $O(|S|)$ and $O(|V|)$ operations. Hence summing up for all $p_i \in P^-$ gives complexity $O(|P| \cdot |S|)$, considering $|V|$ is usually very small compared to $|S|$ and $|P|$. Standardizing \mathbf{Cove} and \mathbf{Unif} , as well as sorting, each take $O(|P|)$ operations. Taking into account that the procedure repeats for a maximum of $|V|$ times, the overall complexity of Algorithm 1 can be expressed as $O(|S| \cdot |P| \cdot |V|)$. Fig. 8 validates this complexity empirically by illustrating the impact of different set sizes $|P|$, $|S|$ and $|V|$ on the running time of Coverage Axis++. In contrast, Coverage Axis requires an exponential cost in the worst case. Although modern solvers accelerate the solving process, long computation time is incurred in the worst case; See Tab. 1.

Flexibility. Coverage Axis++ offers control over the number of selected inner points compared to Coverage Axis. In Sec. 6.1, we explore its robustness to various target numbers of selected skeletal points. This ability to specify a specific number of skeletal points is crucial for learning-based methods, ensuring compatibility with algorithms that assume a fixed number of input points. Unlike Coverage Axis, which enforces a hard constraint in Eq.2 requiring $\mathbf{Dv} \geq \mathbf{1}$, Coverage Axis++ relaxes this constraint, enhancing robustness to coverage conditions. This relaxation is particularly advantageous when dealing with a large number of surface samples. Coverage Axis++ maintains a high coverage rate of the original shape, as demonstrated in Appendix. A.2. Notably, Coverage Axis++ does not impose strict requirements on the watertightness or manifoldness of the input, making it versatile for handling meshes and point

Table 1. Quantitative comparison on run time and shape approximation error between Coverage Axis and Coverage Axis++. The inputs are meshes and point clouds. **Time**: Runtime measured in seconds. $|V|$: The number of skeletal points. \vec{e} : One-sided HD from surface to reconstruction. \overleftarrow{e} : One-sided HD from reconstruction to surface. \overleftrightarrow{e} : Two-sided HD between original surface and reconstruction.

Model	$ V $	Mesh								Point Cloud							
		Coverage Axis				Coverage Axis++				Coverage Axis				Coverage Axis++			
		Time	\vec{e}	\overleftarrow{e}	\overleftrightarrow{e}	Time	\vec{e}	\overleftarrow{e}	\overleftrightarrow{e}	Time	\vec{e}	\overleftarrow{e}	\overleftrightarrow{e}	Time	\vec{e}	\overleftarrow{e}	\overleftrightarrow{e}
Bear-1	68	12.6	3.964%	4.107%	4.107%	1.7	3.846%	4.047%	4.047%	14.1	4.707%	6.031%	6.031%	3.3	5.092%	6.016%	6.016%
Bear-2	49	2.3	4.345%	5.016%	5.016%	1.0	4.313%	4.572%	4.572%	3.6	8.220%	8.103%	8.220%	2.3	3.739%	4.531%	4.531%
Bird	83	>1000	2.879%	2.861%	2.879%	2.3	2.306%	2.560%	2.560%	>1000	3.166%	6.810%	6.810%	3.9	2.590%	2.561%	2.590%
Bug	137	14.4	4.632%	4.586%	4.632%	5.4	3.114%	4.511%	4.511%	16.2	9.208%	8.366%	9.208%	7.5	8.262%	4.398%	8.262%
Bunny	73	2.1	7.625%	7.634%	7.634%	1.5	4.860%	5.771%	5.771%	3.4	6.391%	11.398%	11.398%	3.0	4.324%	6.091%	6.091%
Camel	93	38.5	3.487%	6.420%	6.420%	2.5	2.175%	5.556%	5.556%	40.0	8.340%	7.552%	8.340%	4.1	3.706%	5.108%	5.108%
Chair	115	>1000	2.113%	2.119%	1.903%	4.5	2.035%	2.947%	2.947%	>1000	3.210%	4.199%	4.199%	6.2	3.160%	2.890%	3.160%
Crab-1	93	17	2.546%	2.592%	2.592%	2.9	2.744%	2.608%	2.744%	18.5	3.476%	3.232%	3.476%	4.5	2.862%	3.207%	3.207%
Crab-2	107	16.4	2.901%	2.593%	2.901%	4.0	2.825%	2.767%	2.825%	17.9	3.221%	3.878%	3.878%	5.7	2.764%	2.778%	2.778%
Cup	243	>1000	9.840%	6.031%	9.840%	13.8	9.247%	6.251%	9.247%	>1000	6.658%	7.214%	7.214%	16.4	6.701%	3.809%	6.701%
Dinosaur	66	2.4	2.903%	2.896%	2.903%	1.4	2.308%	2.672%	2.672%	3.8	1.978%	2.175%	2.175%	2.8	2.920%	3.287%	3.287%
Dolphin	30	14.1	16.926%	42.999%	42.999%	0.7	4.916%	15.323%	15.323%	15.3	16.840%	42.768%	42.768%	2.1	6.652%	21.393%	21.393%
Elephant	94	2.9	3.216%	3.525%	3.525%	2.4	3.373%	3.874%	3.874%	4.4	3.519%	3.732%	3.732%	4.0	3.395%	6.155%	6.155%
Fandisk	127	401.8	5.012%	4.597%	5.012%	4.6	3.849%	4.067%	4.067%	403.3	11.310%	9.870%	11.310%	6.3	3.503%	4.298%	4.298%
Femur	26	2.0	2.288%	2.272%	2.288%	0.4	2.314%	3.095%	3.095%	3.4	4.703%	4.953%	4.953%	2.0	2.231%	3.010%	3.010%
Fish	43	41.4	3.686%	9.077%	9.077%	1.1	3.421%	4.809%	4.809%	42.7	7.824%	12.980%	12.980%	2.5	3.627%	4.155%	4.155%
Giraffe	71	2.8	1.914%	2.396%	2.396%	1.7	1.831%	4.208%	4.208%	4.3	4.389%	3.260%	4.389%	3.2	2.727%	3.975%	3.975%
Guitar	71	>1000	2.255%	2.182%	2.255%	1.7	2.136%	2.497%	2.497%	>1000	2.072%	2.276%	2.276%	3.3	4.054%	2.426%	4.054%
Hand	47	11.2	2.104%	2.074%	2.104%	1.1	1.974%	1.975%	1.975%	12.4	8.900%	8.428%	8.900%	5.9	2.237%	2.328%	2.328%
Human	46	2.2	1.827%	1.906%	1.906%	0.9	2.062%	2.105%	2.105%	3.4	2.425%	3.247%	3.247%	2.3	1.959%	6.961%	6.961%
Kitten	148	5.0	5.804%	6.679%	6.679%	5.0	5.839%	7.798%	7.798%	6.6	7.415%	7.941%	7.941%	6.8	7.415%	7.941%	7.941%
Lifebuoy	33	1.5	2.856%	2.251%	2.856%	0.5	3.324%	3.217%	3.324%	2.8	5.252%	4.645%	5.252%	1.9	3.700%	3.669%	3.700%
Neptune	53	3.0	5.947%	11.030%	11.030%	1.2	3.227%	9.989%	9.989%	4.5	4.768%	14.161%	14.161%	2.8	5.435%	5.485%	5.485%
Octopus	74	0.4	2.556%	3.339%	3.339%	1.8	2.696%	3.005%	3.005%	1.7	2.488%	3.231%	3.231%	3.5	2.618%	3.214%	3.214%
Plane	44	64.4	4.660%	10.032%	10.032%	1.0	2.534%	4.306%	4.306%	65.9	4.594%	17.325%	17.325%	2.4	3.704%	4.500%	4.500%
Pot	90	79.8	4.376%	3.562%	4.376%	2.3	3.979%	5.278%	5.278%	81.2	3.631%	5.043%	5.043%	3.6	3.548%	3.726%	3.726%
Rapter	44	10.6	7.073%	14.310%	14.310%	1.0	4.089%	10.727%	10.727%	12.0	5.062%	18.442%	18.442%	2.4	7.425%	9.307%	9.307%
Rocker	112	>1000	3.660%	2.721%	3.660%	3.5	3.652%	3.274%	3.652%	>1000	5.099%	5.736%	5.736%	5.1	3.570%	2.989%	3.570%
Seahorse	60	37.6	2.236%	3.164%	3.164%	1.4	2.296%	5.168%	5.168%	39.0	3.197%	5.592%	5.592%	2.9	2.256%	5.878%	5.878%
Spectacles	97	>1000	2.238%	2.319%	2.319%	2.8	2.323%	3.080%	3.080%	>1000	1.984%	2.395%	2.395%	4.3	2.329%	2.921%	2.921%
Spider	54	3.8	4.629%	5.295%	5.295%	1.1	2.731%	4.493%	4.493%	5.3	5.144%	25.817%	25.817%	2.8	4.532%	5.555%	5.555%
Vase	118	1.1	3.779%	5.971%	5.971%	3.3	3.575%	3.875%	3.875%	2.9	4.199%	6.034%	6.034%	5.2	4.069%	5.006%	5.006%
Wine glass	278	>1000	21.310%	11.724%	21.310%	16.7	22.851%	8.828%	22.851%	>1000	13.673%	8.254%	13.673%	19.2	13.868%	5.952%	13.868%
Average	-	236.1	4.775%	6.069%	6.574%	2.9	3.902%	4.826%	5.362%	237.7	5.669%	8.639%	8.974%	4.6	4.272%	5.016%	5.537%

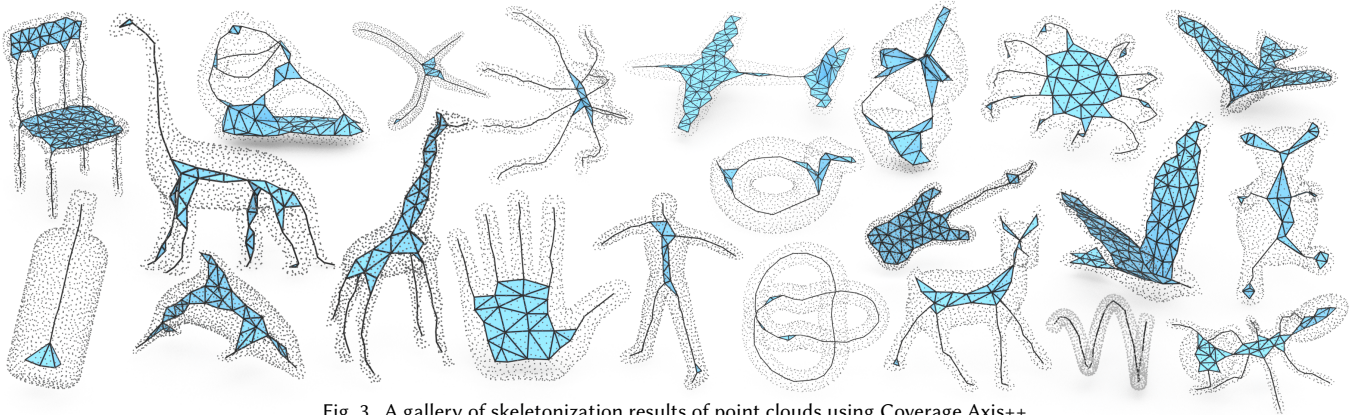


Fig. 3. A gallery of skeletonization results of point clouds using Coverage Axis++.

clouds. Additionally, our method only requires few hyperparameters, namely weight parameter ω , target skeletal number $|V|$, and dilation factor δ_r .

5 EXPERIMENTAL RESULTS

We conduct extensive qualitative and quantitative evaluations of the proposed method to demonstrate its effectiveness comprehensively. We implemented and experimented on a computer with a 4.00 GHz

Intel(R) Core(TM) i7-6700K CPU and 32 GB memory. The sizes of all the models are normalized to the $[0, 1]$ range.

Given the target skeletal point number, Coverage Axis++ only includes two hyperparameters: δ_r (Eq. 4) and ω (Eq. 9). All the experimental results are generated using a consistent parameter setting, i.e., for all kinds of input, we always set $\delta_r = 0.02$ and $\omega = 1$. In experiments where we compare our method with Coverage Axis, we set the number of selected points $|V|$ for Coverage Axis++ to



Fig. 4. Qualitative comparison with SAT. (a-c) SAT. (d) Coverage Axis. (e) Coverage Axis++.

be equal to the number obtained from the SCP solution for the Coverage Axis. We provide additional analyses on parameters δ_r and $|V|$ in Sec. 6. For a fair comparison, we always randomly generate candidate points inside the volume and set the number of surface samples S to be 1500 in all the comparisons. We employ fast winding number [Barill et al. 2018] for inside-outside determination.

We employ the two-sided Hausdorff distance (HD) for assessing consistency between the original and reconstructed surfaces. We use $\vec{\epsilon}$ for surface-to-reconstruction HD, $\overleftarrow{\epsilon}$ for reconstruction-to-surface HD, and $\overleftrightarrow{\epsilon}$ for two-sided HD. The reconstructed surfaces are obtained by interpolating medial balls based on skeleton connectivity, akin to [Dou et al. 2022; Li et al. 2015; Wang et al. 2022b]. Errors are normalized by the diagonal length of the input model

bounding box. In quantitative results, the best results for runtime and accuracy are indicated with blue and orange highlighting, respectively. A gallery of skeletonization results of mesh and point cloud inputs are shown in Fig. 1 and Fig. 3, respectively.

Comparison with Coverage Axis [Dou et al. 2022]. As Coverage Axis can handle both mesh and point cloud inputs, we compared the proposed method with it on both two inputs. We solve SCP (Eq. 2) involved in Coverage Axis using Mixed-integer linear programming (MILP) solver in Matlab (MathWorks 2021). The quantitative results are summarized in Tab. 1. As can be observed, for both mesh and point cloud inputs, Coverage Axis++ achieves higher reconstruction accuracy on most shapes while maintaining competitive accuracy



Fig. 5. Comparison with existing shape skeletonization methods for point clouds.

on the remaining shapes. Moreover, it significantly outperforms the Coverage Axis in terms of running time, where ours achieves 5.362% reconstruction error in 2.9s on average, whereas the Coverage Axis achieves 6.574% reconstruction error in more than 236.1s. The same advantage is also reflected in point cloud inputs. For Coverage Axis, the running times are even longer when using more surface samples; See Appendix. A.1. The qualitative comparison is given in Fig. 5.

Comparison with Q-MAT [Li et al. 2015]. We compare with another representative method Q-MAT. Note that Q-MAT requires a watertight mesh input and cannot handle point clouds or polygon soups. Tab. 2 shows that Coverage Axis++ performs comparably or superior to Q-MAT in terms of reconstruction accuracy and running time. As revealed in [Dou et al. 2022], Q-MAT heavily depends on input mesh quality and the initial Voronoi diagram for computing the medial axis skeleton. In contrast, we use randomly generated candidates inside the volume for Coverage Axis++ in all comparisons, and our method effectively selects the most expressive ones from overfilled inner point candidates.

Table 2. Quantitative comparison on run time and shape approximation error between Q-MAT and Coverage Axis++. The inputs are meshes.

Model	V	Q-MAT				Coverage Axis++			
		Time (s)	$\bar{\epsilon}$	$\bar{\epsilon}$	$\bar{\epsilon}$	Time (s)	$\bar{\epsilon}$	$\bar{\epsilon}$	$\bar{\epsilon}$
Armadillo	82	9.8	2.736%	5.678%	5.678%	1.8	3.615%	5.106%	5.106%
Bear-1	68	5.3	2.732%	3.278%	3.278%	1.7	3.846%	4.047%	4.047%
Bear-2	49	1.6	3.133%	3.089%	3.133%	1.0	4.313%	4.572%	4.572%
Bird	83	2.3	2.361%	3.936%	3.936%	2.3	2.306%	2.560%	2.560%
Bunny	73	16.6	3.474%	4.686%	4.686%	1.5	4.860%	5.771%	5.771%
Camel	93	2.8	2.204%	2.468%	2.468%	2.5	2.175%	5.556%	5.556%
Cup	243	4.6	7.434%	10.841%	10.841%	13.8	9.247%	6.251%	9.247%
Dinosaur	66	8.1	1.930%	2.444%	2.444%	1.4	2.308%	2.672%	2.672%
Dog	69	1.3	2.299%	3.781%	3.781%	1.5	3.353%	3.799%	3.799%
Fandisk	127	2.9	4.888%	5.840%	5.840%	4.6	3.849%	4.067%	4.067%
Femur	26	2.0	2.288%	2.272%	2.288%	0.4	2.314%	3.095%	3.095%
Giraffe	71	2.9	1.278%	3.890%	3.890%	1.7	1.831%	4.208%	4.208%
Hand	47	21.9	1.441%	1.087%	1.441%	1.1	1.974%	1.975%	1.975%
Horse	81	22.9	1.973%	3.683%	3.683%	1.9	2.382%	2.658%	2.658%
Human	46	1.6	2.006%	2.155%	2.155%	0.9	2.062%	2.105%	2.105%
Neptune	53	5.0	2.379%	11.372%	11.372%	1.2	3.227%	9.989%	9.989%
Rapter	44	7.9	3.548%	13.196%	13.196%	1.0	4.089%	10.727%	10.727%
Seahorse	60	7.6	1.908%	4.731%	4.731%	1.4	2.296%	5.168%	5.168%
Vase	118	6.2	2.826%	4.839%	4.839%	3.3	3.575%	3.875%	3.875%

Table 3. Comparison on shape approximation errors among Point2Skeleton (P2S), Deep Point Consolidation (DPC), Coverage Axis and Coverage Axis++.

Model	P2S		DPC		Coverage Axis		Coverage Axis++	
	$ V $	ϵ	$ V $	ϵ	$ V $	ϵ	$ V $	ϵ
Ant-2	100	16.412%	1194	8.863%	58	2.350%	58	2.113%
Bottle	100	2.955%	1194	2.752%	14	2.956%	14	2.599%
Chair-2	100	6.552%	1194	4.807%	89	2.890%	89	3.012%
Dog	100	6.047%	1194	5.237%	49	2.174%	49	2.306%
Dolphin	100	5.925%	1194	7.916%	49	1.971%	49	1.876%
Fertility	100	8.162%	1194	4.226%	79	3.428%	79	3.102%
Guitar	100	2.052%	1194	3.231%	60	2.032%	60	2.344%
Hand-1	100	9.672%	1194	4.110%	44	3.441%	44	2.328%
Kitten	100	8.724%	1194	5.332%	50	3.450%	50	2.962%
Snake	100	15.021%	1194	1.736%	40	1.309%	40	1.402%
Average	-	8.003%	-	4.815%	-	2.515%	-	2.404%

Comparison with SAT [Miklos et al. 2010]. SAT encounters a major drawback as it tends to favor a dense representation with numerous vertices, hindering the generation of a simple and compact skeleton of the given shape. Note SAT only excels specifically with watertight surface meshes. We test with different scaling factors, $\alpha = 1.1, 1.5,$ and 2.0 , revealing that with a smaller α , SAT achieves high accuracy but results in a representation with a large number of vertices (Fig.4(a-c)). Using a larger α for higher abstraction compromises shape structure and introduces significant approximation errors. As a comparison, Coverage Axis++ achieves a balance between fidelity, efficiency, and compression abilities.

Comparison with Deep Point Consolidation [Wu et al. 2015]. As shown in Fig. 5 and Tab. 3, DPC can only produce unstructured inner points without connections and the reconstruction results exhibit large errors. Even worse, the reconstructed topologies by DPC are usually inconsistent with the original input. In contrast, our reconstruction results reach better approximation accuracy with respect to the original geometry using fewer skeletal points.

Comparison with Point2Skeleton [Lin et al. 2021]. Compared with Point2Skeleton [Lin et al. 2021], a learning-based skeletonization method for point clouds, our approach exhibits better performance. As shown in Fig. 5 and Tab. 3, Point2Skeleton, trained on a large dataset ShapeNet [Chang et al. 2015], falls short on shapes unseen during training and struggles with higher topology complexity. However, our method demonstrates robustness, generating high-quality skeletal representations with accurate geometries and faithful structures across diverse shapes.

6 ABLATION STUDY

6.1 Skeletal Point Number

In Sec.4.6, we highlight Coverage Axis++'s practical benefit of flexible specification for the target number of skeletal points. Fig.6 presents our experiments with different target skeletal numbers using three models and three choices of $|V|$. Larger values of $|V|$ result in a more accurate skeletal representation, as observed in the experiments where reconstruction error consistently decreases with increasing $|V|$. However, choosing excessively large $|V|$ contradicts our objective of generating a simple and compact skeleton for shape abstraction. Our results show that specifying a smaller number of skeletal points (e.g., 30 or 50) achieves simpler shape abstraction

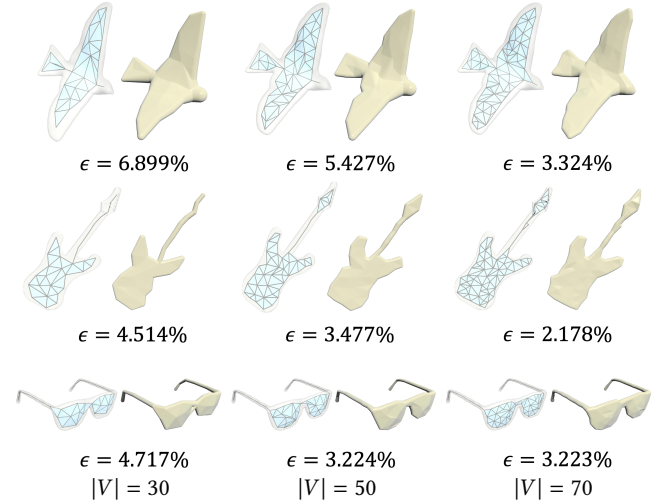
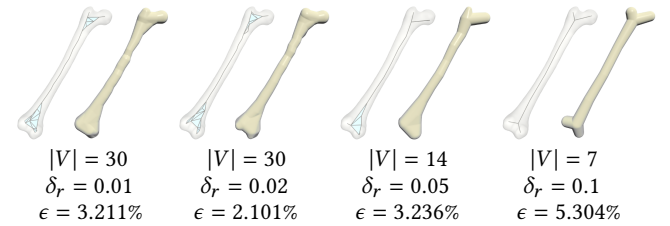
Fig. 6. Influence of target numbers $|V|$. We test our model with the target numbers being 30, 50 and 70.

Fig. 7. Skeletonization results using different dilation offsets.

with only a slight increase in reconstruction error. The flexibility allows users to tailor the method for either a simple or more accurate model, depending on the requirement for shape abstraction.

6.2 Dilation Factor

Next, we perform an ablation study on the dilation factor δ_r using the Femur model as an example. As shown in Fig. 7, increasing δ_r allows balls to cover more surface samples, simplifying the skeletal representation. We always set $|V| = 30$ in Algorithm 1, but when δ_r is 0.05 or larger, the algorithm terminates with fewer than 30 selected points as dilated balls already cover all surface samples. A larger δ_r simplifies the representation but sacrifices geometric details, compromising shape structure preservation. Conversely, an excessively small δ_r contradicts simplicity and compactness. We maintain consistency by setting δ_r to 0.02 in all experiments, balancing geometric details and skeletal compactness.

6.3 Running Time Analysis

The overall complexity of Algorithm 1 is $O(|S| \cdot |P| \cdot |V|)$. Next, we validate the complexity using different set sizes $|P|$, $|S|$ and $|V|$ on the running time of our method. As shown in Fig. 8, Coverage Axis++ has polynomial complexity relationships among various variables, maintaining overall low computational costs.

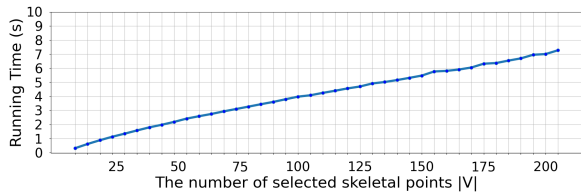
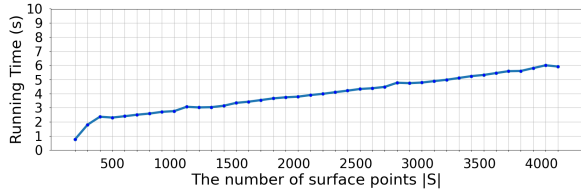
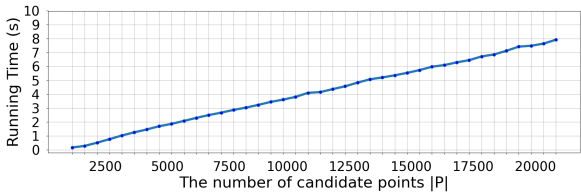
(a) Running time w.r.t. target skeletal point numbers $|V|$ with $|S| = 2000$, $|P| = 10000$.(b) Running time w.r.t. surface sample numbers $|S|$ with $|V| = 100$, $|P| = 10000$.(c) Running time w.r.t. candidate skeletal point numbers $|P|$ with $|V| = 100$, $|S| = 2000$.

Fig. 8. Runtime performance w.r.t. different parameter settings.

7 DISCUSSION AND CONCLUSION

In this paper, we present Coverage Axis++, an efficient shape skeletonization method. Unlike existing methods that depend on input watertightness or suffer from high computational costs, Coverage Axis++ addresses these challenges by employing a heuristic algorithm considering both shape coverage and centrality for selecting skeletal points, which ensures an efficient approximation of the MAT while significantly saving the computational cost. Compared with existing methods, our simple yet effective approach produces a compact representation of MAT, offers versatility in skeletonizing various shape representations, allows customizable specification of skeletal points, and achieves highly efficient computation with improved reconstruction accuracy. Extensive experiments across diverse 3D shapes demonstrate the efficiency and effectiveness of Coverage Axis++.

REFERENCES

Nina Amenta, Sungho Choi, and Ravi Krishna Kolluri. 2001. The power crust. In *Proceedings of the sixth ACM symposium on Solid modeling and applications*. 249–266.

Daniel Cohen-Or, Andrea Tagliasacchi, Hao Zhang. 2009. Curve skeleton extraction from incomplete point cloud. *ACM Transactions on Graphics (Proc. SIGGRAPH)* 28, 3 (2009), 71:1–71:9.

Dominique Attali, Jean-Daniel Boissonnat, and Herbert Edelsbrunner. 2009. Stability and computation of medial axes—a state-of-the-art report. In *Mathematical foundations of scientific visualization, computer graphics, and massive data exploration*. Springer, 109–125.

Dominique Attali and Anick Montanvert. 1996. Modeling noise for a better simplification of skeletons. In *Proceedings of 3rd IEEE International Conference on Image Processing*, Vol. 3. IEEE, 13–16.

Oscar Kin-Chung Au, Chiew-Lan Tai, Hung-Kuo Chu, Daniel Cohen-Or, and Tong-Yee Lee. 2008. Skeleton extraction by mesh contraction. *ACM transactions on graphics (TOG)* 27, 3 (2008), 1–10.

Franz Aurenhammer. 1987. Power diagrams: properties, algorithms and applications. *SIAM J. Comput.* 16, 1 (1987), 78–96.

Andreas Bærentzen and Eva Rotenberg. 2021. Skeletonization via local separators. *ACM Transactions on Graphics (TOG)* 40, 5 (2021), 1–18.

Ilya Baran and Jovan Popović. 2007. Automatic rigging and animation of 3d characters. *ACM Transactions on graphics (TOG)* 26, 3 (2007), 72–es.

Gavin Barill, Neil G Dickson, Ryan Schmidt, David IW Levin, and Alec Jacobson. 2018. Fast winding numbers for soups and clouds. *ACM Transactions on Graphics (TOG)* 37, 4 (2018), 1–12.

Harry Blum et al. 1967. *A transformation for extracting new descriptors of shape*. Vol. 43. MIT press Cambridge, MA.

Junjie Cao, Andrea Tagliasacchi, Matt Olson, Hao Zhang, and Zhinxun Su. 2010. Point cloud skeletons via laplacian based contraction. In *2010 Shape Modeling International Conference*. IEEE, 187–197.

Angel X Chang, Thomas Funkhouser, Leonidas Guibas, Pat Hanrahan, Qixing Huang, Zimo Li, Silvio Savarese, Manolis Savva, Shuran Song, Hao Su, et al. 2015. Shapenet: An information-rich 3d model repository. *arXiv preprint arXiv:1512.03012* (2015).

John Chaussard, Michel Couprie, and Hugues Talbot. 2011. Robust skeletonization using the discrete λ -medial axis. *Pattern Recognition Letters* 32, 9 (2011), 1384–1394.

Frédéric Chazal and André Lieutier. 2005. The “ λ -medial axis”. *Graphical Models* 67, 4 (2005), 304–331.

Jingliang Cheng, Xinyu Zheng, Shuangmin Chen, Guozhu Liu, Shiqing Xin, Lin Lu, Yuanfeng Zhou, and Changhe Tu. 2020. Skeletonization via dual of shape segmentation. *Computer Aided Geometric Design* 80 (2020), 101856.

Tamal K Dey, Herbert Edelsbrunner, Sumanta Guha, and Dmitry V Nekhayev. 1998. Topology preserving edge contraction. In *Publ. Inst. Math.(Beograd)(NS. Citeaser*.

Tamal K Dey and Jian Sun. 2006. Defining and computing curve-skeletons with medial geodesic function. In *Symposium on geometry processing*, Vol. 6. 143–152.

Tamal K Dey and Wulue Zhao. 2002. Approximate medial axis as a Voronoi subcomplex. In *Proceedings of the seventh ACM symposium on Solid modeling and applications*. 356–366.

Zhiyang Dou, Cheng Lin, Rui Xu, Lei Yang, Shiqing Xin, Taku Komura, and Wenping Wang. 2022. Coverage axis: Inner point selection for 3d shape skeletonization. In *Computer Graphics Forum*, Vol. 41. Wiley Online Library, 419–432.

Zhiyang Dou, Shiqing Xin, Rui Xu, Jian Xu, Yuanfeng Zhou, Shuangmin Chen, Wenping Wang, Xiuyang Zhao, and Changhe Tu. 2020. Top-down shape abstraction based on greedy pole selection. *IEEE Transactions on Visualization and Computer Graphics* 27, 10 (2020), 3982–3993.

Noura Faraj, Jean-Marc Thiery, and Tamy Boubekeur. 2013. Progressive medial axis filtration. In *SIGGRAPH Asia 2013 Technical Briefs*. 1–4.

Mark Foskey, Ming C Lin, and Dinesh Manocha. 2003. Efficient computation of a simplified medial axis. *J. Comput. Inf. Sci. Eng.* 3, 4 (2003), 274–284.

Zhiying Fu, Rui Xu, Shiqing Xin, Shuangmin Chen, Changhe Tu, Chenglei Yang, and Lin Lu. 2022. Easyvrmodeling: Easily create 3d models by an immersive vr system. *Proceedings of the ACM on Computer Graphics and Interactive Techniques* 5, 1 (2022), 1–14.

Michael Garland and Paul S Heckbert. 1997. Surface simplification using quadric error metrics. In *Proceedings of the 24th annual conference on Computer graphics and interactive techniques*. 209–216.

Mengyuan Ge, Junfeng Yao, Baorong Yang, Ningna Wang, Zhonggui Chen, and Xiaohu Guo. 2023. Point2MM: Learning medial mesh from point clouds. *Computers & Graphics* 115 (2023), 511–521.

Joachim Giesen, Balint Miklos, Mark Pauly, and Camille Wormser. 2009. The scale axis transform. In *Proceedings of the twenty-fifth annual symposium on Computational geometry*. 106–115.

Juris Hartmanis. 1982. Computers and intractability: a guide to the theory of np-completeness (michael r. Garey and david s. Johnson). *Siam Review* 24, 1 (1982), 90.

Jianwei Hu, Gang Chen, Baorong Yang, Ningna Wang, Xiaohu Guo, and Bin Wang. 2022. IMMAT: Mesh reconstruction from single view images by medial axis transform prediction. *Computer-Aided Design* 150 (2022), 103304.

Jianwei Hu, Ningna Wang, Baorong Yang, Gang Chen, Xiaohu Guo, and Bin Wang. 2023. S3DS: Self-supervised Learning of 3D Skeletons from Single View Images. In *Proceedings of the 31st ACM International Conference on Multimedia*. 6948–6958.

Hui Huang, Shihao Wu, Daniel Cohen-Or, Minglun Gong, Hao Zhang, Guiqing Li, and Baoquan Chen. 2013. L1-medial skeleton of point cloud. *ACM Trans. Graph.* 32, 4 (2013), 65–1.

Pan Li, Bin Wang, Feng Sun, Xiaohu Guo, Caiming Zhang, and Wenping Wang. 2015. Q-MAT: Computing medial axis transform by quadratic error minimization. *ACM Transactions on Graphics (TOG)* 35, 1 (2015), 1–16.

- Cheng Lin, Changjian Li, Yuan Liu, Nenglu Chen, Yi-King Choi, and Wenping Wang. 2021. Point2Skeleton: Learning skeletal representations from point clouds. In *Proceedings of the IEEE/CVF Conference on Computer Vision and Pattern Recognition*. 4277–4286.
- Cheng Lin, Lingjie Liu, Changjian Li, Leif Kobbelt, Bin Wang, Shiqing Xin, and Wenping Wang. 2020. SEG-MAT: 3D shape segmentation using medial axis transform. *IEEE Transactions on Visualization and Computer Graphics* (2020).
- Guying Lin, Lei Yang, Congyi Zhang, Hao Pan, Yuhang Ping, Guodong Wei, Taku Komura, John Keyser, and Wenping Wang. 2023. Patch-Grid: An Efficient and Feature-Preserving Neural Implicit Surface Representation. *arXiv preprint arXiv:2308.13934* (2023).
- Yaron Lipman, Daniel Cohen-Or, David Levin, and Hillel Tal-Ezer. 2007. Parameterization-free projection for geometry reconstruction. *ACM Transactions on Graphics (TOG)* 26, 3 (2007), 22–es.
- Hsueh-Ti Derek Liu, Mark Gillespie, Benjamin Chislett, Nicholas Sharp, Alec Jacobson, and Keenan Crane. 2023b. Surface simplification using intrinsic error metrics. *ACM Transactions on Graphics (TOG)* 42, 4 (2023), 1–17.
- Zhen Liu, Yao Feng, Yuliang Xiu, Weiyang Liu, Liam Paull, Michael J Black, and Bernhard Schölkopf. 2023a. Ghost on the Shell: An Expressive Representation of General 3D Shapes. *arXiv preprint arXiv:2310.15168* (2023).
- Marco Livesu, Fabio Guggeri, and Riccardo Scateni. 2012. Reconstructing the curve-skeletons of 3d shapes using the visual hull. *IEEE transactions on visualization and computer graphics* 18, 11 (2012), 1891–1901.
- Wan-Chun Ma, Fu-Che Wu, and Ming Ouhyoung. 2003. Skeleton extraction of 3D objects with radial basis functions. In *2003 Shape Modeling International*. IEEE, 207–215.
- Romain Marie, Ouiddad Labbani-Igbida, and El Mustapha Mouaddib. 2016. The delta medial axis: a fast and robust algorithm for filtered skeleton extraction. *Pattern Recognition* 56 (2016), 26–39.
- Zoë Marschner, Silvia Sellán, Hsueh-Ti Derek Liu, and Alec Jacobson. 2023. Constructive Solid Geometry on Neural Signed Distance Fields. In *SIGGRAPH Asia 2023 Conference Papers*. 1–12.
- Balint Miklos, Joachim Giesen, and Mark Pauly. 2010. Discrete scale axis representations for 3D geometry. In *ACM SIGGRAPH 2010 papers*. 1–10.
- Mattia Natali, Silvia Biasotti, Giuseppe Patanè, and Bianca Falcidieno. 2011. Graph-based representations of point clouds. *Graphical Models* 73, 5 (2011), 151–164.
- Daniel Rebain, Baptiste Angles, Julien Valentin, Nicholas Vining, Jiju Peethambaran, Shahram Izadi, and Andrea Tagliasacchi. 2019. LSMAT Least squares medial axis transform. In *Computer Graphics Forum*, Vol. 38. Wiley Online Library, 5–18.
- Daniel Rebain, Ke Li, Vincent Sitzmann, Soroosh Yazdani, Kwang Moo Yi, and Andrea Tagliasacchi. 2021. Deep medial fields. *arXiv preprint arXiv:2106.03804* (2021).
- Silvia Sellán, Noam Aigerman, and Alec Jacobson. 2021. Swept volumes via spacetime numerical continuation. *ACM Transactions on Graphics (TOG)* 40, 4 (2021), 1–11.
- Silvia Sellán, Jacob Kesten, Ang Yan Sheng, and Alec Jacobson. 2020. Opening and closing surfaces. *ACM Transactions on Graphics (TOG)* 39, 6 (2020), 1–13.
- Andrei Sharf, Thomas Lewiner, Ariel Shamir, and Leif Kobbelt. 2007. On-the-fly Curve-skeleton Computation for 3D Shapes. In *Computer Graphics Forum*, Vol. 26. Wiley Online Library, 323–328.
- Wei Shen, Xiang Bai, Rong Hu, Hongyuan Wang, and Longin Jan Latecki. 2011. Skeleton growing and pruning with bending potential ratio. *Pattern Recognition* 44, 2 (2011), 196–209.
- Jamie Shotton, Andrew Fitzgibbon, Mat Cook, Toby Sharp, Mark Finocchio, Richard Moore, Alex Kipman, and Andrew Blake. 2011. Real-time human pose recognition in parts from single depth images. In *CVPR 2011*. Ieee, 1297–1304.
- Svetlana Stolpner, Paul Kry, and Kaleem Siddiqi. 2011. Medial spheres for shape approximation. *IEEE transactions on pattern analysis and machine intelligence* 34, 6 (2011), 1234–1240.
- Avneesh Sud, Mark Foskey, and Dinesh Manocha. 2007. Homotopy-preserving medial axis simplification. *International Journal of Computational Geometry & Applications* 17, 05 (2007), 423–451.
- Feng Sun, Yi-King Choi, Yizhou Yu, and Wenping Wang. 2013. Medial meshes for volume approximation. *arXiv preprint arXiv:1308.3917* (2013).
- Andrea Tagliasacchi, Ibraheem Alhashim, Matt Olson, and Hao Zhang. 2012. Mean curvature skeletons. In *Computer Graphics Forum*, Vol. 31. Wiley Online Library, 1735–1744.
- Andrea Tagliasacchi, Thomas Delame, Michela Spagnuolo, Nina Amenta, and Alexandru Telea. 2016. 3d skeletons: A state-of-the-art report. In *Computer Graphics Forum*, Vol. 35. Wiley Online Library, 573–597.
- Jiapeng Tang, Xiaoguang Han, Junyi Pan, Kui Jia, and Xin Tong. 2019. A skeleton-bridged deep learning approach for generating meshes of complex topologies from single rgb images. In *Proceedings of the IEEE/CVF Conference on Computer Vision and Pattern Recognition*. 4541–4550.
- Ningna Wang, Bin Wang, Wenping Wang, and Xiaohu Guo. 2022a. Computing medial axis transform with feature preservation via restricted power diagram. *ACM Transactions on Graphics (TOG)* 41, 6 (2022), 1–18.
- Pengfei Wang, Zixiong Wang, Shiqing Xin, Xifeng Gao, Wenping Wang, and Changhe Tu. 2022b. Restricted delaunay triangulation for explicit surface reconstruction. *ACM Transactions on Graphics* 41, 5 (2022), 1–20.
- Cheng Wen, Baosheng Yu, and Dacheng Tao. 2023. Learnable Skeleton-Aware 3D Point Cloud Sampling. In *Proceedings of the IEEE/CVF Conference on Computer Vision and Pattern Recognition*. 17671–17681.
- Shihao Wu, Hui Huang, Minglu Gong, Matthias Zwicker, and Daniel Cohen-Or. 2015. Deep points consolidation. *ACM Transactions on Graphics (ToG)* 34, 6 (2015), 1–13.
- Shi-Qing Xin, Bruno Lévy, Zhonggui Chen, Lei Chu, Yaohui Yu, Changhe Tu, and Wenping Wang. 2016. Centroidal power diagrams with capacity constraints: Computation, applications, and extension. *ACM Transactions on Graphics (TOG)* 35, 6 (2016), 1–12.
- Rui Xu, Zhiyang Dou, Ningna Wang, Shiqing Xin, Shuangmin Chen, Mingyan Jiang, Xiaohu Guo, Wenping Wang, and Changhe Tu. 2023. Globally consistent normal orientation for point clouds by regularizing the winding-number field. *ACM Transactions on Graphics (TOG)* 42, 4 (2023), 1–15.
- Rui Xu, Zixiong Wang, Zhiyang Dou, Chen Zong, Shiqing Xin, Mingyan Jiang, Tao Ju, and Changhe Tu. 2022. RFEPS: Reconstructing feature-line equipped polygonal surface. *ACM Transactions on Graphics (TOG)* 41, 6 (2022), 1–15.
- Zhan Xu, Yang Zhou, Evangelos Kalogerakis, and Karan Singh. 2019. Predicting animation skeletons for 3d articulated models via volumetric nets. In *2019 International Conference on 3D Vision (3DV)*. IEEE, 298–307.
- Yajie Yan, David Letscher, and Tao Ju. 2018. Voxel Cores: Efficient, robust, and provably good approximation of 3d medial axes. *ACM Transactions on Graphics (TOG)* 37, 4 (2018), 1–13.
- Yajie Yan, Kyle Sykes, Erin Chambers, David Letscher, and Tao Ju. 2016. Erosion thickness on medial axes of 3D shapes. *ACM Transactions on Graphics (TOG)* 35, 4 (2016), 1–12.
- Baorong Yang, Junfeng Yao, and Xiaohu Guo. 2018. DMAT: Deformable medial axis transform for animated mesh approximation. In *Computer Graphics Forum*, Vol. 37. Wiley Online Library, 301–311.
- Baorong Yang, Junfeng Yao, Bin Wang, Jianwei Hu, Yiling Pan, Tianxiang Pan, Wenping Wang, and Xiaohu Guo. 2020. P2MAT-Net: Learning medial axis transform from sparse point clouds. *Computer Aided Geometric Design* 80 (2020), 101874.
- Lei Yang, Yongqing Liang, Xin Li, Congyi Zhang, Guying Lin, Alla Sheffer, Scott Schaefer, John Keyser, and Wenping Wang. 2023. Neural parametric surfaces for shape modeling. *arXiv preprint arXiv:2309.09911* (2023).
- Yiding Yang, Zhou Ren, Haoxiang Li, Chunluan Zhou, Xinchao Wang, and Gang Hua. 2021. Learning dynamics via graph neural networks for human pose estimation and tracking. In *Proceedings of the IEEE/CVF Conference on Computer Vision and Pattern Recognition*. 8074–8084.
- Lior Yariv, Omri Puny, Natalia Neverova, Oran Gafni, and Yaron Lipman. 2023. Mosaic-SDF for 3D Generative Models. *arXiv preprint arXiv:2312.09222* (2023).
- Zhengming Yu, Zhiyang Dou, Xiaoxiao Long, Cheng Lin, Zekun Li, Yuan Liu, Norman Müller, Taku Komura, Marc Habermann, Christian Theobalt, et al. 2023. Surf-D: High-Quality Surface Generation for Arbitrary Topologies using Diffusion Models. *arXiv preprint arXiv:2311.17050* (2023).
- Congyi Zhang, Guying Lin, Lei Yang, Xin Li, Taku Komura, Scott Schaefer, John Keyser, and Wenping Wang. 2023. Surface Extraction from Neural Unsigned Distance Fields. In *Proceedings of the IEEE/CVF International Conference on Computer Vision*. 22531–22540.

A APPENDIX

This supplementary material covers: more experimental results (Sec. A.1), coverage rate of Coverage Axis++ (Sec. A.2), computation complexity analysis on Coverage Axis (Sec. A.3) as well as limitations and future works (Sec. A.4).

A.1 More Experimental Results

As discussed in Sec. 4.6, the proposed method has polynomial complexity with respect to the number of surface samples, denoted as $|S|$. In contrast, the Coverage Axis algorithm showcases exponential complexity in $|S|$. This is evidenced by Tab. 1 of the main paper, where we report the running times of our method and Coverage Axis for various models when $|S|$ is set to 1500. Furthermore, it can be expected that when increasing the number of surface samples, the performance gap between our method and the Coverage Axis will widen further. We conducted additional experiments by increasing the number of surface samples to 5000 and comparing the performance of our method with the Coverage Axis across different shapes. The results are summarized in Tab. A5.

Note that the proportion of timeout models (i.e., models with a running time exceeding 1000s) of Coverage Axis increases from 21.2% to 50% as $|S|$ increases from 1500 to 5000. Furthermore, comparing the results obtained with $|S|$ set as 1500 and 5000, we find that Coverage Axis++ exhibits a more significant advantage over Coverage Axis in terms of running time. On average, our method achieves a reconstruction error of 4.429% in 9.7s, whereas Coverage Axis achieves a reconstruction error of 5.448% in over 516.3s.

A.2 Coverage Rate

In the main paper, we conducted extensive experiments for Coverage Axis++ on various models to demonstrate that our method is capable of extracting compact underlying shape representation of MAT while achieving low reconstruction error, as summarized in Tab. 1. Since the selected skeletal points form a good representation of the medial axis, the corresponding dilated balls should cover a significant portion of the surface samples to build the correspondence between the medial balls and the shape volume. In other words, the coverage rate of our method should be high. The idea has been verified by Coverage Axis, as it directly requires a 100% coverage rate by imposing a hard constraint during the optimization. We record the coverage rates of each model for Coverage Axis++, which are summarized in Tab. A4. The result shows that our method consistently achieves very high coverage rates, with an average of 96.134%.

A.3 Complexity Analysis on Coverage Axis

Next, we provide more analysis of the complexity of the Coverage Axis. From Tab. 1 of the main paper, we observe that the running times of the Coverage Axis for certain models (such as Bird, Chair, Guitar, and Spectacles) are extremely long, indicating that solving SCP (Eq. 2) for these models is particularly challenging. Note that a common characteristic of these shapes is that they all have planar shapes. We illustrate why solving SCP for models with planar shapes is difficult.

Table A4. Coverage rate of Coverage Axis++. The inputs are meshes. $|V|$: The number of skeletal points. $\overleftrightarrow{\epsilon}$: Two-sided HD between original surface and reconstruction.

Model	$ V $	$\overleftrightarrow{\epsilon}$	Coverage rate
Bear-1	68	4.047%	98.662%
Bear-2	49	4.572%	98.461%
Bird	83	2.560%	95.914%
Bug	137	4.511%	98.274%
Bunny	73	5.771%	97.650%
Camel	93	5.556%	96.919%
Chair	115	2.947%	96.082%
Crab-1	93	2.744%	97.874%
Crab-2	107	2.825%	98.608%
Cup	243	9.247%	95.411%
Dinosaur	66	2.672%	99.331%
Elephant	94	3.874%	98.079%
Fandisk	127	4.067%	92.029%
Femur	26	3.095%	97.536%
Fish	43	4.809%	88.587%
Giraffe	71	4.208%	97.335%
Guitar	71	2.497%	96.804%
Hand	47	1.975%	95.143%
Human	46	2.105%	98.869%
Lifebuoy	33	3.324%	96.151%
Octopus	74	3.005%	97.989%
Plane	44	4.306%	83.389%
Pot	90	5.278%	95.786%
Rocker	112	3.652%	96.944%
Seahorse	60	5.168%	96.144%
Spectacles	97	3.080%	96.075%
Spider	54	4.493%	95.987%
Vase	118	3.875%	95.710%
Average	-	3.938%	96.134%

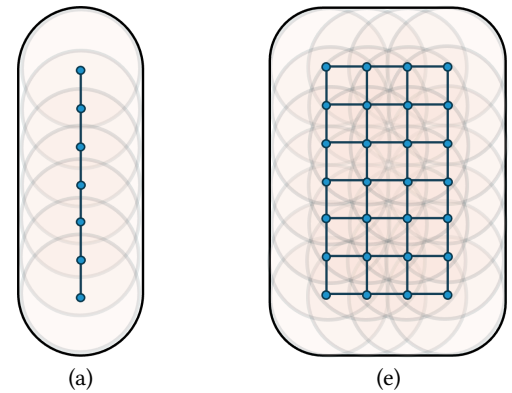


Fig. A9. Distribution of randomly sampled candidate skeletal points in two different shapes. (a) tubular structure. (b) planar structure.

Given an arbitrary shape, under the meaning of medial axis transform, it can be divided into two types of shapes: *tubular* and *planar* structures, as depicted in Fig. A9. Without loss of generality, we assume that the size and sample density of the two shapes are the same. In such cases, if the tubular shape contains q points, the planar shape would have q^2 points. In the SCP formulation, the 0-1 decision vector \mathbf{v} in Eq. 2 of the main paper is defined in a way that

Table A5. Quantitative comparison on run time and shape approximation error between Coverage Axis and Coverage Axis++ when the number of surface samples is set as 5000. The inputs are meshes. **Time**: Runtime measured in seconds. $|V|$: The number of skeletal points. $\vec{\epsilon}$: One-sided HD from surface to reconstruction. $\overleftarrow{\epsilon}$: One-sided HD from reconstruction to surface. $\overleftrightarrow{\epsilon}$: Two-sided HD between original surface and reconstruction.

Model	$ V $	Coverage Axis			Coverage Axis++				
		Time	$\overleftarrow{\epsilon}$	$\overleftrightarrow{\epsilon}$	Time	$\overleftarrow{\epsilon}$	$\overleftrightarrow{\epsilon}$		
Bear-1	70	115.2	3.651%	4.958%	4.958%	5.1	2.752%	2.795%	2.795%
Bear-2	38	7.5	7.412%	7.385%	7.412%	2.5	4.552%	5.997%	5.997%
Bird	101	>1000	1.959%	1.857%	1.959%	9.8	2.177%	2.438%	2.438%
Bug	145	>1000	5.701%	5.636%	5.701%	12.2	3.074%	3.005%	3.074%
Camel	116	25.6	2.488%	2.238%	2.488%	9.5	2.513%	2.936%	2.936%
Chair	137	>1000	1.920%	1.871%	1.920%	13.6	1.909%	2.105%	2.105%
Crab-1	92	43.9	3.738%	3.293%	3.738%	9.5	2.577%	2.738%	2.738%
Crab-2	83	210.5	7.705%	6.223%	7.705%	8.9	3.168%	3.212%	3.212%
Cup	286	>1000	9.176%	5.026%	9.176%	27.8	9.174%	6.390%	9.174%
Dog	65	7.6	4.557%	4.386%	4.557%	5.0	2.642%	2.876%	2.876%
Elephant	89	147.1	6.015%	7.221%	7.221%	8.5	3.168%	3.925%	3.925%
Fandisk	210	>1000	2.925%	2.778%	2.925%	23.7	2.613%	3.057%	3.057%
Femur	27	13.6	2.842%	2.782%	2.842%	2.0	2.035%	2.035%	2.035%
Fish	72	>1000	1.769%	2.271%	2.271%	5.7	1.994%	2.722%	2.722%
Giraffe	50	25.9	5.841%	5.853%	5.853%	5.1	2.627%	5.267%	5.267%
Guitar	63	>1000	2.040%	4.312%	4.312%	7.4	2.232%	2.383%	2.383%
Hand	46	131.4	2.874%	2.607%	2.874%	4.2	3.315%	2.884%	3.315%
Horse	56	200.2	5.174%	6.042%	6.042%	4.6	3.608%	5.246%	5.246%
Lifebuoy	38	96.7	4.667%	4.196%	4.667%	2.8	2.52%	3.307%	3.307%
Neptune	120	206.8	2.115%	5.751%	5.751%	11.4	3.128%	5.542%	5.542%
Pig	51	16.6	8.535%	8.575%	8.575%	3.5	6.038%	8.327%	8.327%
Plane	84	>1000	1.708%	2.275%	2.275%	8.7	1.965%	2.533%	2.533%
Pliers	32	13.5	2.072%	1.925%	2.072%	2.8	2.081%	2.055%	2.081%
Pot	152	>1000	3.570%	3.100%	3.570%	14.4	3.504%	3.690%	3.690%
Rapter	74	>1000	3.322%	6.545%	6.545%	6.2	3.322%	6.634%	6.634%
Rocker	130	>1000	3.632%	3.496%	3.632%	14.4	3.777%	2.790%	3.777%
Seahorse	53	>1000	2.763%	11.156%	11.156%	4.8	2.288%	5.515%	5.515%
Spectacles	112	>1000	1.982%	1.952%	1.982%	14.4	1.660%	1.653%	1.660%
Vase	109	226.1	5.260%	6.587%	6.587%	9.2	3.132%	3.192%	3.192%
Wine-glass	335	>1000	22.680%	7.904%	22.680%	34.6	21.310%	8.549%	21.310%
Average	-	516.3	4.670%	4.673%	5.448%	9.7	3.695%	3.860%	4.429%

each entry indicates whether the corresponding candidate point is selected. Consequently, for the tubular shape, there are 2^q possible combinations, while for the planar shape, there are 2^{q^2} possible combinations. As a result, solving the SCP becomes significantly more challenging when the model involves planar shapes due to the exponential increase in the number of possible combinations. In comparison, Coverage Axis++ sidesteps solving an optimization problem with high computation complexity by designing a simple yet effective heuristic algorithm, taking coverage and uniformity into consideration, which thus achieves significant acceleration.

A.4 Limitations and Future Works

Coverage Axis++ approximates the whole shape by an abstraction of local geometry with the union of the local geometries forming the entire shape. One limitation of Coverage Axis++ is that its whole process is conducted without a hard constraint forcing the consistency between the selected medial balls and the shape surface (See coverage rate statistics in Sec. A.2), like that in Coverage Axis [Dou et al. 2022]. Although local approximation has been evidenced by some previous works [Amenta et al. 2001; Ge et al. 2023; Lin et al.

2021], we acknowledge that the inclusion of a global constraint imposes a much stricter guarantee for the shape correspondence.

Another limitation is that as we keep the whole pipeline in a neat format, the uniformity of the skeletonization achieved by the Coverage Axis++ can occasionally be slightly inferior compared to that of the Coverage Axis. In future work, the uniformity scoring term in Algorithm 1 of the main paper can be further improved.